FEBS Letters

Nucleotide-dependent conformational changes of the AAA+ ATPase p97 revisited

Jan M. Schuller[1], Florian Beck[1], Philip Lössl[2], Albert J. R. Heck[2] and Friedrich Förster[1]

1 Department of Molecular Structural Biology, Max-Planck Institute of Biochemistry, Martinsried, Germany
2 Biomolecular Mass Spectrometry and Proteomics and Netherlands Proteomics Center, Bijvoet Center for Biomolecular Research and Utrecht Institute for Pharmaceutical Sciences, Utrecht University, The Netherlands

Correspondence
F. Förster, Department of Molecular Structural Biology, Max-Planck Institute of Biochemistry, D-82152 Martinsried, Germany
Fax: +49 89 8578 2641
Tel: +49 89 8578 2632
E-mail: foerster@biochem.mpg.de

(Received 26 January 2016, revised 28 January 2016, accepted 1 February 2016, available online 20 February 2016)

doi:10.1002/1873-3468.12091

Edited by Peter Brzezinski

The ubiquitous AAA-ATPase p97 segregates ubiquitylated proteins from their molecular environment. Previous studies of the nucleotide-dependent conformational changes of p97 were inconclusive. Here, we determined its structure in the presence of ADP, AMP-PNP, or ATP-γS at 6.1–7.4 Å resolution using single particle cryo-electron microscopy. Both AAA domains, D1 and D2, assemble into essentially six-fold symmetrical rings. The pore of the D1-ring remains essentially closed under all nucleotide conditions, whereas the D2-ring shows an iris-like opening for ADP. The largest conformational changes of p97 are 'swinging motions' of the N-terminal domains, which may enable segregation of ubiquitylated substrates from their environment.

Keywords: AAA-ATPase; Cdc48; Cryo-EM; ERAD; protein quality control

The type II AAA+ protein p97/Cdc48 (mammalian/yeast) is a chaperone-like molecular machine that utilizes the chemical energy released by ATP hydrolysis for segregation of ubiquitylated proteins from their environment, such as protein complexes and membranes [1,2]. P97 copies assemble into homohexameric complexes, which acquire substrate and processing specificity through a large number of transiently associating cofactors [1,3,4]. Single amino acid mutations in human p97 (also referred to as VCP) have been linked to neurodegenerative disorders, such as inclusion body myopathy associated with Paget disease of bone and frontotemporal dementia (IBMPFD) [5].

P97 consists of an N-terminal effector binding domain (N-domain) and two AAA domains (D1 and D2). X-ray crystallographic studies revealed the architecture of these domains in the homohexameric complex [6–8]. D1 and D2 both form six-fold homohexameric rings, which are stacked on top of each other in a 'head-to-tail' arrangement. This symmetrical arrangement is in contrast to some other AAA-ATPases, including the closely related N-ethylmaleimide sensitive factor (NSF) [9], which adopt staircase-like topologies that undergo changes during their nucleotide cycles. In the full-length X-ray crystallographic structures, the structural differences of the AAA domains of p97 are comparatively small between the different nucleotide states [7,8]. In all full-length structures, the centers of mass of the N-domains are arranged essentially coplanar with those of D1. However, the positioning of the N-domain differs in the X-ray structure of the N-D1 fragment carrying the IBMPFD associated point mutations (R155H or A232E) in the presence of ATP-γS, in which the centers of mass of the N-domains resides significantly above the plane of the centers of mass of D1 [10,11].

Abbreviations
EM, electron microscopy; FCR, Fourier cross-resolution; IBMPFD, inclusion body myopathy associated with Paget disease of bone and frontotemporal dementia; MS, mass spectrometry; NSF, N-ethylmaleimide sensitive factor; SAXS, small-angle X-ray scattering.

While the present X-ray crystallographic structures provide accurate structural information about the single domain structures, the quaternary structure observed in the crystals might not be physiological. Low-resolution small-angle X-ray scattering (SAXS) [12], atomic force microscopy [13] and cryo-electron microscopy (EM) studies [14,15] all suggest much larger conformational differences between the different nucleotide states than observed in the full-length X-ray crystallographic structures. A likely source for the discrepancy between the scales of motion observed in the crystallographic and solution data are the extensive contacts between the D2 and N-domains of adjacent particles in the crystal lattices [7,8]. In particular, the positions of the N-domains seem to be strongly biased by the crystal packing. However, due to insufficient resolution, solution studies have so far failed to conclusively address the precise domain positions and their internal rearrangements for the different nucleotide states.

In this study, we revisit the conformational landscape of p97 in the presence of three nucleotides, AMP-PNP, ATP-γS, and ADP, using cryo-EM single particle analysis and recent advances in electron detector technology [16,17].

Material and methods

Sample preparation

Full-length p97 was purified as described previously [7]. About 4 μL of purified protein was applied to a lacey carbon copper grid (Quantifoil, Groβlöbichau, Germany), incubated for 30 s, manually blotted with filter paper and washed two times with 4 μL buffer (containing the respective nucleotide) and 0.05% NP40, before final blotting and vitrification in liquid ethane.

Mass spectrometry

P97 was buffer exchanged to 150 mM $CH_3CO_2NH_4$ pH 7.5 (for native MS) or 0.1% (v/v) HCOOH (for MS under denaturing conditions) using Micro Bio-Spin P30 columns (Bio-Rad, Hercules, CA, USA). To study nucleotide binding by native MS, p97 was incubated with 1 mM of the respective nucleotide and 1 mM $MgCl_2$ for 30 min at room temperature prior to buffer exchange. The buffer exchanged samples were loaded in gold-coated borosilicate capillaries and were analyzed by nano-electrospray ionization-MS at a protein concentration of 4–5 μM using a modified Orbitrap Exactive Plus EMR mass spectrometer (Thermo Scientific, Waltham, MA, USA), externally calibrated with CsI clusters [18]. The following instrument settings were used for native MS: capillary voltage = 1.3–1.4 kV, source fragmentation voltage = 20 V, S-lens extraction voltage = 150–200 V, HCD energy = 50 V, N_2 gas pressure in HCD cell = 7×10^{-10} bar, mass resolution at 200 m/z = 6000. For MS under denaturing condition, the energy and gas pressure in the HCD cell were set to minimum. The mass spectra were analyzed with XCALIBUR v2.2 and the mass of denatured p97 was determined using PROTEIN DECONVOLUTION v3.0 (both Thermo Scientific).

Electron microscopy

All data were collected on a 300 keV FEI Titan Krios electron microscope equipped with a K2 Summit detector (Gatan, Pleasanton, CA, USA) operated in counting mode (10 e^- $pixel^{-1}\cdot s^{-1}$, 30 frames with a total dose of 40 $e^-/Å^{2-}$). The data sets of p97-AMP-PNP and p97-ADP were collected at a magnification of 81 000× (1.74 $Å\cdot pixel^{-1}$), whereas the p97-ATP-γS data were collected at 105 000× magnification (1.35 $Å\cdot pixel^{-1}$). TOM^2 automated acquisition software [19] was used to collect a total of 2464 (p97-AMP-PNP), 3276 (p97-ADP) and 1728 (p97-ATP-γS) micrographs.

Image analysis

From micrographs that did not show astigmatism or strong drift particles were selected automatically [20]. CTF parameter determination was carried out on the whole micrograph level using *ctffind3* [21]. All subsequent processing of the particles was carried out in *RELION*. To evaluate conformational heterogeneity 3D classification was carried out using 50 classes. For subsequent analysis we aligned the protomers of the 50 classes based on the pseudo six-fold rotational symmetries (Fig. S2), resulting in 300 volumes. The densities inside the mask encapsulating the N-domain of one protomer (approximately 4 nm in diameter) were then analyzed statistically by principal component analysis of the correlation matrix and subsequent hierarchical clustering according to the first eigenvector in TOM [22]. For the AMP-PNP, ADP, and ATP-γS datasets, resolutions of 9.3, 9, and 8.1 Å were determined, respectively. The nonsymmetrized maps were subjected to rotational correlation analysis in TOM [22]. Subsequently, six-fold rotational symmetry was imposed for a final refinement round increasing the resolution to 7.4, 6.8, and 6.1 Å for AMP-PNP, ADP, and ATP-γS datasets, respectively. The local resolution was computed using Bsoft [23], and the maps were filtered accordingly. The EM densities have been deposited in the EMDataBank for the ADP state (EMDB-3323, EMDB-3326), AMP-PNP state (EMD-3324, EMDB-3328), and ATP-γS state (EMD-3325, EMDB-3327). Molecular graphics and analyses were performed with the UCSF CHIMERA package [24]. The consistency of all fits was analyzed by Fourier cross-resolution of the reconstruction and the density simulated from the atomic model in TOM [22].

Results

Characterization and data acquisition of pre- and posthydrolysis states

To correlate our data with prior structural data and biochemical characterization we used incubated purified p97 with three extensively studied nucleotides: (a) The posthydrolysis state was induced by adding excess ADP to the buffer ('ADP dataset') [7,14,15]. Biochemical studies indicate that all 12 nucleotide binding sites of the p97 hexamer have ADP molecules bound under the conditions of the experiment [12]. (b) To mimic an ATP-bound state the nonhydrolysable ATP-analog AMP-PNP has often been employed [7,12,14]. However, the affinity of AMP-PNP for p97 is much lower than that of ATP and ADP [25]. For our experimental conditions, approximately five ADP and five AMP-PNP molecules have been detected per p97 particle [12]. (c) The slowly hydrolysable analog ATP-γS is an alternative means to lock a prehydrolysis state. The affinity of ATP-γS is comparable to that of ATP and biochemical studies indicate that 9–10 ATP-γS nucleotides are bound per p97 molecule under the conditions of the sample [26].

Prior to structural analysis, we characterized the nucleotide states of our samples after purification and in the presence of ADP and ATP-γS by native mass spectrometry (MS) [27,28]. AMP-PNP was omitted in this experiment due to the anticipated strong heterogeneity of nucleotide states, which is not to be easily resolved by native MS. To determine the precise mass of apo p97 its monomeric mass was first measured after denaturation (Fig. S1A). The most abundant peak among four species is a form that likely corresponds to p97, which has been acetylated after removal of the N-terminal Met-Gly. Because each of the four monomeric species may be incorporated in the p97 hexamer, their weighted mass average was used to calculate the averaged expected mass of the hexameric apo p97 (548 491 Da).

We then aimed to analyze to which extent nucleotides remain prebound to p97 after recombinant expression and purification in nucleotide-free buffer. The major population in the recorded spectra corresponds to hexameric p97 with 10 ADP molecules bound (Fig. S1B). Upon incubation with ADP the spectrum indicates that the major mode becomes loaded with 11 ADP molecules (Fig. 1A). In both cases, only distinct ADP loading states are present, suggesting cooperative nucleotide binding.

When purified p97 was incubated with ATP-γS the spectra indicate exchange of the prebound ADP by ATP-γS. As a result, the major subspecies is shifted to higher molecular weights, indicating that the prebound ADP has been fully or partially replaced by ATP-γS (Fig. 1C). Assuming complete exchange of ADP by ATP-γS, the most abundant species can be assigned to p97 with 10 Mg^{2+}-ATP-γS bound, again indicating cooperative nucleotide exchange and binding (Fig. 1B).

Conformational variability at different nucleotide conditions

Because statistical distribution of different monomer conformers within the homohexameric ring can give rise to a large number of different overall configurations, we classified each dataset into 50 different 3D classes. To identify the major monomer conformers we subsequently superposed the protomers of the ring-shaped class reconstructions according to their respective rotations around their six-fold pseudosymmetry axis in the center of the molecule and subjected them to hierarchical clustering focusing on an area encompassing their N-domains (Fig. S2A).

For the ADP dataset, this analysis indicates that the computed reconstructions from the ADP dataset are highly similar to each other and hence conformational heterogeneity is negligible (Fig. S2B). In all classes, the centers of mass of all N-domains are in plane with those of the D1 domain ('down' state in the following) akin to the X-ray crystallographic structures of full-length p97 [7].

In contrast, the analysis of the N-domain positioning indicates heterogeneity for the AMP-PNP dataset. The monomers adopt two preferred conformations that mostly differ in the positioning of the N-domains (Fig. S2C): their centers of mass position either above the plane of the centers of mass of the D1 domains ('up' state in the following) or in the 'down' state. In addition to these two major conformers, the classification reveals another less populated and less-defined class that resembles the up-state. This class corresponding to a 'background' of heterogeneous conformations ('flexible' state) is not considered in the further analysis. In contrast to the positions of the N-domains, the AAA domains do not show notable differences. For the ATP-γS dataset the classification reveals that only very few monomers adopt a defined up-conformation (Fig. S2D). The most populated classes show the N-domain also in a 'flexible' upward position, but much more washed-out, or the N-domain is not resolved at all. Thus, the conformational space of the N-domain is considerably larger in the presence of ATP-γS than for AMP-PNP and ADP and it primarily

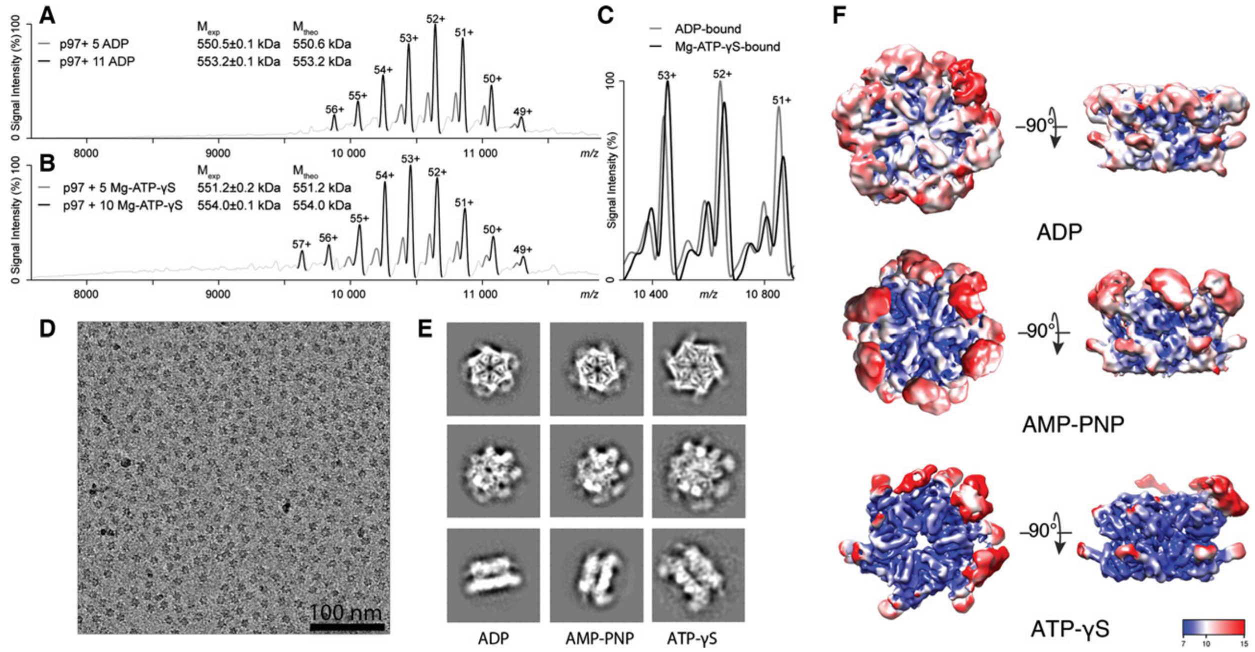

Fig. 1. Native MS and Cryo-EM single particle analysis of p97 after incubation with different nucleotides. (A) Broad-range native mass spectrum of ADP-bound p97. The peaks are labeled with their respective charge states. Listed are the experimentally determined masses ± standard deviation (M_{exp}) and the theoretical masses (M_{theo}) of the identified species, which were calculated based on the mass of apo-p97 (Fig. S1A. (B) Broad-range native mass spectrum of Mg-ATP-γS-bound p97. (C) Overlay of three charge states representing ADP- and Mg-ATP-γS-bound p97. All peaks are shifted to higher *m/z* values upon incubation with Mg-ATP-γS. (D) Part of a cryo-EM micrograph of p97 in presence of ATP-γS. The bar corresponds to 100 nm. (E) Reference-free 2D class averages from three data sets with p97 bound to different nucleotides. (F) Side- and top-views of the ADP-, AMP-PNP-, and ATP-γS-bound structures, which are colored according to their local resolution.

contains upward facing states. In contrast to the ADP and AMP-PNP datasets, the down-conformer is entirely absent in the ATP-γS dataset.

Subnanometer resolution reconstructions with and without imposed six-fold symmetry

As the ADP data were found to be structurally homogeneous, we merged the particles from the best-resolved classes, yielding an 8.4 Å resolution reconstruction (Fig. 1F, Figs S3 and S5). To investigate the symmetry of the AAA core, we masked out the N-domains and computed the rotational autocorrelation function, which showed pronounced peaks at multiples of 60° (Fig. S4). This analysis indicates that the AAA core is essentially identical upon six-fold rotation to a resolution of 9 Å coinciding with the FSC estimate for the reconstruction. Subtle differences in the densities of the N-domains of the individual protomers are not significant at the lower local resolution, which does not reach subnanometer level (Fig. S3). Thus, at the resolution determined here no deviations from six-fold symmetry can be discerned, which does not exclude the possibility of subtle deviations at higher resolutions. Hence, we realigned the particles with imposed six-fold rotational symmetry (C_6) resulting in a 6.9 Å resolution 'ADP density' (Fig. 2 and Fig. S5).

Among the classes representing the AMP-PNP dataset, a class with 'all-up' N-domains clearly yields the highest resolution indicating that the corresponding particles have the highest degree of homogeneity. From the ~ 20 000 particles contributing to the all-up class we obtained a reconstruction of 9.3 Å resolution (Fig. 1F, Figs S3 and S5). The symmetry analysis of the AAA core and N-domain again indicates six-fold symmetry at the achieved resolution (Fig. 1F and Fig. S4). Accordingly, we imposed six-fold symmetry for final alignment of these particles, which improved the resolution to 7.5 Å (Fig. 2 and Fig. S5).

As the N-domains in the ATP-γS data were determined to be structurally heterogeneous, we subsequently focused the alignment on the AAA core for this dataset. Classification did not indicate structural heterogeneity in the AAA core and the ~ 40 000 particles from the best-resolved classes yielded a reconstruction of 8.1 Å resolution (Fig. 1F, Figs S3 and S5). The

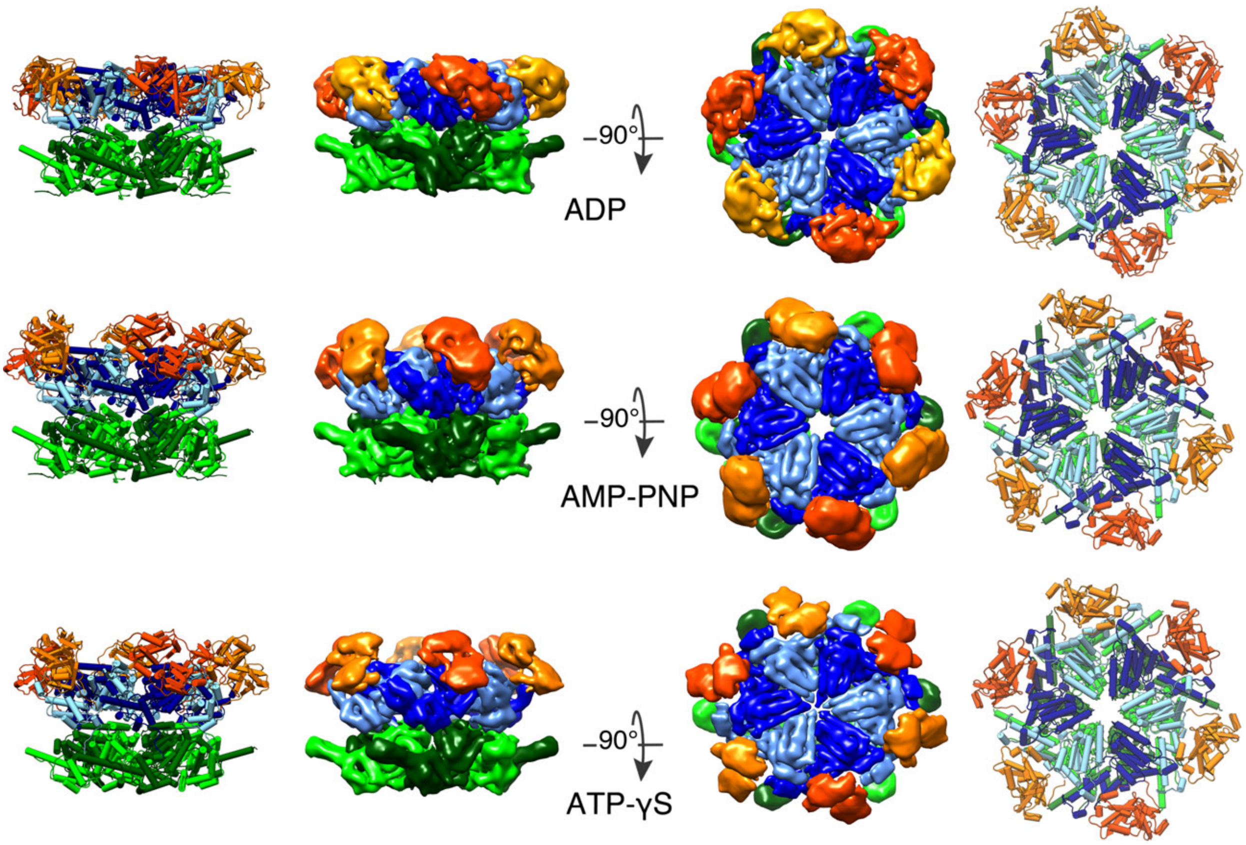

Fig. 2. p97 densities refined with imposed six-fold symmetry and corresponding pseudoatomic models. Center columns: the maps were segmented and colored according to their domains in alternating dark and light color tones. (orange: N-domain, blue: D1 domain, green: D2 domain). Left and right columns: the fitted atomic models are depicted in the same color code.

subsequent symmetry analysis of the AAA core showed six-fold rotational symmetry (Fig. 2, Fig. S4) and the resolution of the refined symmetrized reconstruction improved to 6.1 Å (Fig. 2 and Fig. S5).

Conformational changes of the N-D1 segment

To interpret the structural rearrangements of p97 for the different nucleotides we sought to explain the observed EM density by the existing crystallographic structures. For the ADP densities, the crystal structure of full-length p97 bound to ADP (PDB: 3cf3) yielded the best fit. The Fourier cross-resolution (FCR) of this atomic model with the EM data (6.8 Å) shows that it explains the ADP density to the reported resolution (6.9 Å) (Figs S5 and S6A).

In contrast, the AMP-PNP density and the X-ray crystallographic model of p97 bound to AMP-PNP (PDB: 3cf2) differ substantially, most notably in the positioning of the N-domain. The structures of the IBMPFD associated p97 N-D1 mutants (R155H or A232E) bound to ATP-γS (PDB: 4ko8/4kln) [10], which both have the N-domain positioned at an elevated position, fit the N-D1 segment of the AMP-PNP density best yielding a FCR (7.4 Å), consistent with the resolution estimate (7.5 Å) (Figs S5 and S6B). The crystal structures of the ATP-γS-bound IBMPFD p97 N-D1 mutants with the elevated N-domain also explain the ATP-γS density best, markedly better than the full-length ATP-γS-bound Δ709–728 p97 crystal structure [8] (Fig. 2, Fig. S6C).

The largest structural difference between the N-D1 segments of the cryo-EM ADP- and AMP-PNP/ATP-γS structures is the repositioning of the N-domains: they translate upwards from the D1 ring by 12.5 Å (center of gravity of the domain) and rotate by 90°, resulting in a 'swinging' motion (Fig. 3A). The conformational differences between the D1 domains in the AMP-PNP/ATP-γS and the ADP structures are comparatively small with displacements of the Cα-atoms below 5 Å throughout. The largest changes involve the helices H12 and H13 of the small subdomain of D1, which form a major interface with the N-domain in the ADP state. A notable feature of all D1 conformations observed here is that the D1 pore is extremely narrow, in agreement with the fitted crystal structures.

Limited proteolysis experiments on the IBMPFD p97 mutants have implicated ordering of the N-terminal residues upon ATP binding [29]. Indeed, the AMP-PNP density shows a well-defined density segment (Fig. 3B), for which the fitted atomic model suggests that it corresponds to the very N-terminal residues (residues 1–20). These N-terminal 20 residues are absent from all p97 crystal structures but one protomer of the ATP-γS-bound IBMPFD mutant A232E, which includes residues 12–20 [10]. These eight residues coincide with part of the segment. Tracing it further suggests that the very N-terminus of p97 is positioned between the helices H1 and H2 of the D2 domain and the peptide further traverses adjacent to the loop connecting H12 and H13 of the D1 domain. Thus, our cryo-EM structure confirms that the ATP-induced ordering of the N-termini is a genuine feature of p97.

Conformational changes of the D2 domain

For the ADP and the AMP-PNP D2 ring, the best fitting atomic model is the p97-ADP crystal structure (PDB: 3cf3). The FCRs for this model and the ADP and AMP-PNP maps (6.8 and 7.4 Å, respectively) both match the determined resolution (Fig. S6). The best fit to the ATP-γS D2 cryo-EM density is the ATP-γS-bound Δ709–728 p97 crystal structure (PDB: 5C18, Fig. S6) [8], yielding the FCR for this atomic model and the ATP-γS map (7 Å) is in the range of the determined resolution, indicating that the model

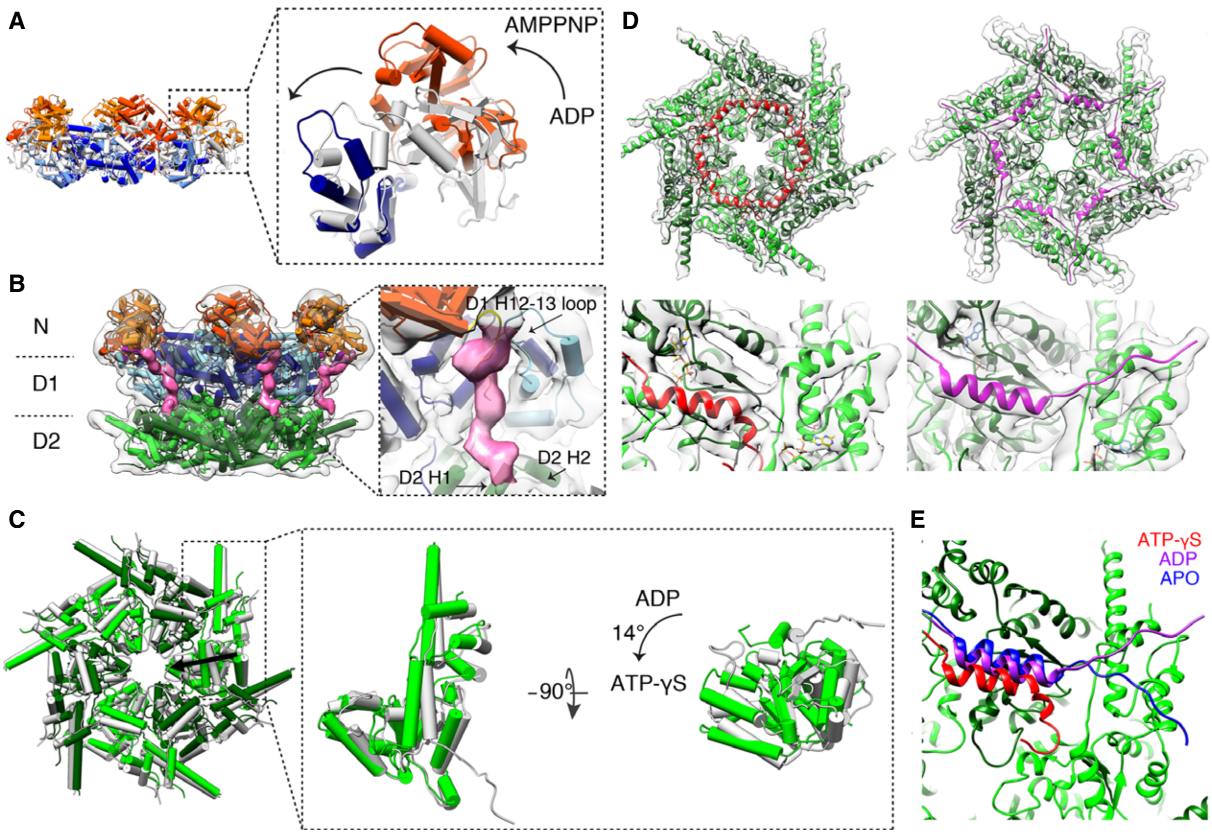

Fig. 3. Structural changes in the domain segments. (A) Structural changes of the AMP-PNP-model (colored) compared to the ADP-model (white). The swinging motion of the N-domain is indicated by an arrow. (B) Visualization of the most N-terminal residues in the AMP-PNP structure (pink). (C) The change of the D2 ring in the presence of ATP-γS compared to ADP can be explained by a rigid body transformation. The green model shows the ATP-γS state, whereas the gray-model displays the ADP state. An arrow for one protomer indicates the tilt axis of its 14° rotation. (D) Visualization of the C-termini in the ATP-γS (red) and ADP (purple) states. (E) Comparison of the conformations of the C-termini in different nucleotide states. In the ATP-γS-bound p97 (red) the C-terminal helix is kinked and points toward p97's central channel. In the ADP bound state (purple) the C-terminus binds to the side of the adjacent D2 small subdomain. In the apo-state (from crystal structure 5C19), the C-terminus binds to the top of the small D2 subdomain.

explains the density well (Fig. S6). Compared to the ADP/AMP-PNP structure, the D2 domain is rotated by approximately 14° along an axis perpendicular to the symmetry axis, narrowing the D2 pore in an aperture-like fashion.

The C-terminal helix of p97 is resolved in all D2 maps. It binds to the small subdomains of the adjacent monomer, similar as in several RecA-type ATPases [30–32]. In the ATP-γS density, the C-terminal helix is kinked and binds in the cleft between the large and small subunits of the neighboring ATPase domain, consistent with the ATP-γS-bound Δ709–728 p97 crystal structure. In addition, to the C-terminal helix, 11 residues are resolved that continue along the bottom of the small D2 subdomain of the adjacent monomer (Fig. 3D). Compared to the ATP-γS state the C-terminus binds at the opposite face of the small D2 subdomain of the neighboring protomer in the ADP/AMP-PNP structure (Fig. 3E).

Discussion

To capture p97 in different steps of its hydrolysis cycle, we analyzed its structure in the presence of in the ATP analogs AMP-PNP and ATP-γS, as well as in the ADP ground state. High-resolution native mass spectrometry was employed to thoroughly characterize the p97 nucleotide loading state in the presence of ADP or ATP-γS, demonstrating that the particles studied by EM were predominantly loaded with either 11 ADP or 10 ATP-γS molecules. Moreover, the high mass resolving power allowed us to observe distinct p97 nucleotide loading states, indicating that nucleotide binding takes place in discrete cooperative steps of 5–6 nucleotides. In agreement with this notion, we could not detect significant deviations from the six-fold symmetry for the AAA core for any of the three nucleotides tested, which clearly distinguishes p97 from the related NSF [9]. Nevertheless, we cannot exclude the possibility of subtle deviations from six-fold symmetry at higher resolutions than those obtained in our study.

As the studied nucleotide states have been investigated previously, we can clarify the partially contradicting structural data on p97. Extensive classification revealed that it is structurally homogeneous in the presence of ADP and its six-fold symmetrical, compact structure is essentially identical to that of full-length p97 determined by X-ray crystallography [7] and SAXS [12]. A relative rotation of the D1 and D2 domains, as described in AFM experiments in the presence of ATP or ADP [13], were not seen in any of the cryo-EM maps determined here.

In the presence of AMP-PNP, the homohexamers adopt heterogeneous conformations. A variety of different hexameric combinations occur that can be attributed to the down protomer state observed in the ADP density and an up-state, in which the centers of mass of the N-domains are positioned above those of the D1-domain. This finding differs from SAXS analysis of the same sample, which suggested that the N-domains are positioned rather further below the D1 domain and move laterally [12]. This discrepancy may be due to the SAXS interpretation inherently assuming homogeneous conformations, whereas our cryo-EM single particle analysis accounts for conformational heterogeneity, which can most likely be attributed to differing occupancies of the low-affinity AMP-PNP and ADP in the particles. The finding that a truncated N-D1 construct binds exclusively AMP-PNP, whereas full-length p97 has similar amounts of AMP-PNP and ADP bound [12] supports the interpretation that N-D1 protomers in the up-state have AMP-PNP bound, whereas the down conformers probably have prebound ADP or no nucleotide bound.

The nonsymmetrized and symmetrized all-up reconstructions are clearly different from the crystal structure of full-length p97 bound to AMP-PNP [7]: the compact X-ray crystallographic conformation is most likely induced by crystal contacts, as also anticipated by the authors [7]. However, the all-up N-D1 conformation in the AMP-PNP map is essentially identical to that in the crystal structures of N-D1 fragments with R155H or A232E mutations bound to ATP-γS [10,11], indicating that the 'up' N-D1 configuration is a generic conformation of p97 and not specific for the IBMPFD mutants. Thus, the IBMPFD mutations rather change the equilibrium of the naturally occurring p97 conformations, in line with previous hypothesis [10,11]. A notable feature of the AMP-PNP structure is the binding of the p97 N-termini to the D2 domains, which apparently stabilizes this configuration.

In the ATP-γS dataset, the down-conformer of the N-domain was not detected, supporting the notion that prebound ADP induces this conformer in the presence of the lower affinity AMP-PNP. Due to high variability, the N-domain is poorly resolved, but it clearly preferably adopts an up-conformation. Consistent with this finding, the D1 domain adopts the same conformation as in the AMP-PNP density. A possible reason for the more variable N-domain positioning is the different conformation of D2, which correlates with the absence of the p97 N-terminus at the D2 domain.

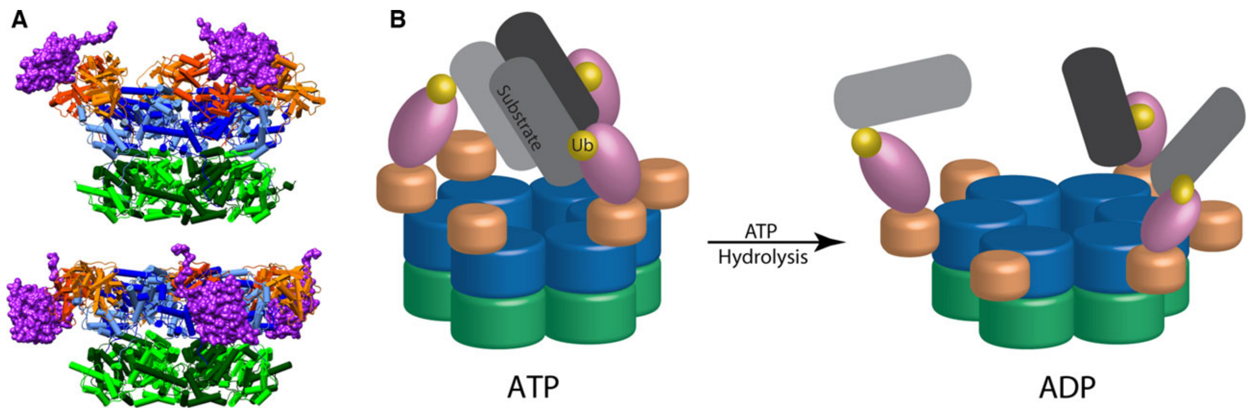

Fig. 4. Model of p97-mediated segregation. (A) The crystal structure of the C-terminal UBX domain of p47 (PDB: 1s3s, purple surface representation) is superimposed onto the p97 AMP-PNP and ADP models. (B) The cartoon indicates the possible positioning of a recruited substrate (gray), such as trimeric SNARE complexes for p47, in the ATP and ADP states. Via their ubiquitin tag (yellow), the substrates bind to the N-terminal domain of p47, which would position them near the pseudosymmetry axis of the D1-domain for the ATP state. The swinging motion of the N-domain upon hydrolysis may then segregate the SNARE monomers from each other and enable further cofactor-mediated substrate processing.

Three different mechanistic models for p97's segregation activity are currently considered in the field [1]: (i) threading of substrates through the central pore of p97, (ii) substrates enter and exit the pore at the D2 end, and (iii) pronounced domain movements of p97 rather than direct involvement of the pore.

The finding that the archaeal p97 homolog VAT can act as an 20S proteasome activator strongly suggests that VAT can thread substrates akin to ATPases of other ATP-dependent proteases [33,34]. In contrast to its archaeal homologs, p97 lacks critical aromatic residues in the D1 pore loop that are required for unfoldase activity in ATP-dependent proteases [35,36]. Contrary to early low-resolution cryo-EM reconstructions [14], the subnanometer p97 structures presented here indicate that the D1 pore remains too narrow to accommodate a peptide during the hydrolysis cycle. Thus, our structures do not corroborate the threading model (i).

The structural differences of the D2 domain observed in the crystal structures of p97 bound to ADP, AMP-PNP, and ATP-γS support the notion that substrates are processed in the interior of the D2 ring [8,37]. Our cryo-EM structures confirm that these conformational changes occur in solution. Hence, our structural data are consistent with substrate processing in the D2 pore (ii).

Our structural data also agree with model (iii): the repositioning of the N-domain as a result of nucleotide hydrolysis may provide the necessary force to disassemble targeted complexes. To illustrate a possible segregation mechanism, we superposed the cocrystal structure of the p97 N-domain with the C-terminal ubiquitin regulatory X domain (UBX) of the substrate-recruiting cofactor p47 [38] onto the atomic ATP-γS and ADP models (Fig. 4A). These superpositions suggest that the substrate recruited by the N-terminal Ubiquitin-Associated domain (UBA) of p47 would be positioned near the D1 cylinder end in the ATP state, which would be analogous to the NSF/SNAP/SNARE supercomplex [9]. The ~ 90° rotation and concomitant ~ 12 Å translation induces a strongly leveraged repositioning of the substrate (Fig. 4B). Thus, the nucleotide-dependent conformational changes observed in this study may explain how substrates are segregated from their binding partners.

Acknowledgements

We thank Michaela Hartwig and Robert Buschauer for assistance in protein purification, Oana Mihalache for help in sample preparation and Benjamin Engel for critically reading the manuscript. This work was supported by the German Research Council GRK1721. P.L and A.J.R.H acknowledge support by the Mani-Fold project (grant agreement number 317371), embedded in the European Union 7th Framework Program, and the Roadmap Initiative Proteins@Work (project number 184.032.201), funded by The Netherlands Organisation for Scientific Research (NWO).

Author contributions

J.S. carried out cryo-EM experiments; J.S., F.B., and F.F. processed and analyzed the EM data; P.L. carried out the native MS experiments; all authors interpreted the results; J.S. and F.F. wrote the paper.

References

1 Buchberger A (2013) Roles of cdc48 in regulated protein degradation in yeast. *Subcell Biochem* **66**, 195–222.
2 Braun S, Matuschewski K, Rape M, Thoms S and Jentsch S (2002) Role of the ubiquitin-selective CDC48 (UFD1/NPL4)chaperone (segregase) in ERAD of OLE1 and other substrates. *EMBO J* **21**, 615–621.
3 Jentsch S and Rumpf S (2007) Cdc48 (p97): a "molecular gearbox" in the ubiquitin pathway? *Trends Biochem Sci* **32**, 6–11.
4 Forster F, Schuller JM, Unverdorben P and Aufderheide A (2014) Emerging mechanistic insights into AAA complexes regulating proteasomal degradation. *Biomolecules* **4**, 774–794.
5 Watts GD, Wymer J, Kovach MJ, Mehta SG, Mumm S, Darvish D, Pestronk A, Whyte MP and Kimonis VE (2004) Inclusion body myopathy associated with Paget disease of bone and frontotemporal dementia is caused by mutant valosin-containing protein. *Nat Genet* **36**, 377–381.
6 DeLaBarre B and Brunger AT (2003) Complete structure of p97/valosin-containing protein reveals communication between nucleotide domains. *Nat Struct Biol* **10**, 856–863.
7 Davies JM, Brunger AT and Weis WI (2008) Improved structures of full-length p97, an AAA ATPase: implications for mechanisms of nucleotide-dependent conformational change. *Structure* **16**, 715–726.
8 Hanzelmann P and Schindelin H (2016) Structural basis of ATP hydrolysis and intersubunit signaling in the AAA+ ATPase p97. *Structure* **24**, 127–139.
9 Zhao M, Wu S, Zhou Q, Vivona S, Cipriano DJ, Cheng Y and Brunger AT (2015) Mechanistic insights into the recycling machine of the SNARE complex. *Nature* **518**, 61–67.
10 Tang WK, Li D, Li CC, Esser L, Dai R, Guo L and Xia D (2010) A novel ATP-dependent conformation in p97 N-D1 fragment revealed by crystal structures of disease-related mutants. *EMBO J* **29**, 2217–2229.
11 Tang WK and Xia D (2013) Altered intersubunit communication is the molecular basis for functional defects of pathogenic p97 mutants. *J Biol Chem* **288**, 36624–36635.
12 Davies JM, Tsuruta H, May AP and Weis WI (2005) Conformational changes of p97 during nucleotide hydrolysis determined by small-angle X-Ray scattering. *Structure* **13**, 183–195.
13 Noi K, Yamamoto D, Nishikori S, Arita-Morioka K, Kato T, Ando T and Ogura T (2013) High-speed atomic force microscopic observation of ATP-dependent rotation of the AAA+ chaperone p97. *Structure* **21**, 1992–2002.
14 Rouiller I, DeLaBarre B, May AP, Weis WI, Brunger AT, Milligan RA and Wilson-Kubalek EM (2002) Conformational changes of the multifunction p97 AAA ATPase during its ATPase cycle. *Nat Struct Biol* **9**, 950–957.
15 Yeung HO, Forster A, Bebeacua C, Niwa H, Ewens C, McKeown C, Zhang X and Freemont PS (2014) Inter-ring rotations of AAA ATPase p97 revealed by electron cryomicroscopy. *Open Biol* **4**, 130142.
16 Bai XC, Fernandez IS, McMullan G and Scheres SH (2013) Ribosome structures to near-atomic resolution from thirty thousand cryo-EM particles. *Elife* **2**, e00461.
17 Li X, Mooney P, Zheng S, Booth CR, Braunfeld MB, Gubbens S, Agard DA and Cheng Y (2013) Electron counting and beam-induced motion correction enable near-atomic-resolution single-particle cryo-EM. *Nat Methods* **10**, 584–590.
18 Rose RJ, Damoc E, Denisov E, Makarov A and Heck AJ (2012) High-sensitivity Orbitrap mass analysis of intact macromolecular assemblies. *Nat Methods* **9**, 1084–1086.
19 Korinek A, Beck F, Baumeister W, Nickell S and Plitzko JM (2011) Computer controlled cryo-electron microscopy–TOM(2) a software package for high-throughput applications. *J Struct Biol* **175**, 394–405.
20 Hrabe T, Beck F and Nickell S (2012) Automated particle picking based on correlation peak shape analysis and iterative classification. *Int J Med Biol Sci* **6**, 1–7.
21 Mindell JA and Grigorieff N (2003) Accurate determination of local defocus and specimen tilt in electron microscopy. *J Struct Biol* **142**, 334–347.
22 Nickell S, Förster F, Linaroudis A, Net WD, Beck F, Hegerl R, Baumeister W and Plitzko JM (2005) TOM software toolbox: acquisition and analysis for electron tomography. *J Struct Biol* **149**, 227–234.
23 Cardone G, Heymann JB and Steven AC (2013) One number does not fit all: mapping local variations in resolution in cryo-EM reconstructions. *J Struct Biol* **184**, 226–236.
24 Goddard TD, Huang CC and Ferrin TE (2007) Visualizing density maps with UCSF chimera. *J Struct Biol* **157**, 281–287.
25 Zalk R and Shoshan-Barmatz V (2003) ATP-binding sites in brain p97/VCP (valosin-containing protein), a multifunctional AAA ATPase. *Biochem J* **374**, 473–480.
26 Briggs LC, Baldwin GS, Miyata N, Kondo H, Zhang X and Freemont PS (2008) Analysis of nucleotide binding to P97 reveals the properties of a tandem AAA hexameric ATPase. *J Biol Chem* **283**, 13745–13752.
27 Snijder J and Heck AJ (2014) Analytical approaches for size and mass analysis of large protein assemblies. *Ann Rev Anal Chem* **7**, 43–64.

28 Heck AJ (2008) Native mass spectrometry: a bridge between interactomics and structural biology. *Nat Methods* **5**, 927–933.
29 Fernandez-Saiz V and Buchberger A (2010) Imbalances in p97 co-factor interactions in human proteinopathy. *EMBO Rep* **11**, 479–485.
30 Whelan F, Stead JA, Shkumatov AV, Svergun DI, Sanders CM and Antson AA (2012) A flexible brace maintains the assembly of a hexameric replicative helicase during DNA unwinding. *Nucleic Acids Res* **40**, 2271–2283.
31 Rzechorzek NJ, Blackwood JK, Bray SM, Maman JD, Pellegrini L and Robinson NP (2014) Structure of the hexameric HerA ATPase reveals a mechanism of translocation-coupled DNA-end processing in archaea. *Nat Commun* **5**, 5506.
32 Byrne RT, Schuller JM, Unverdorben P, Forster F and Hopfner KP (2014) Molecular architecture of the HerA-NurA DNA double-strand break resection complex. *FEBS Lett* **588**, 4637–4644.
33 Barthelme D and Sauer RT (2012) Identification of the Cdc48*20S proteasome as an ancient AAA+ proteolytic machine. *Science* **337**, 843–846.
34 Forouzan D, Ammelburg M, Hobel CF, Stroh LJ, Sessler N, Martin J and Lupas AN (2012) The archaeal proteasome is regulated by a network of AAA ATPases. *J Biol Chem* **287**, 39254–39262.
35 Rothballer A, Tzvetkov N and Zwickl P (2007) Mutations in p97/VCP induce unfolding activity. *FEBS Lett* **581**, 1197–1201.
36 Barthelme D, Chen JZ, Grabenstatter J, Baker TA and Sauer RT (2014) Architecture and assembly of the archaeal Cdc48*20S proteasome. *Proc Natl Acad Sci USA* **111**, 1687–1694.
37 DeLaBarre B, Christianson JC, Kopito RR and Brunger AT (2006) Central pore residues mediate the p97/VCP activity required for ERAD. *Mol Cell* **22**, 451–462.
38 Dreveny I, Kondo H, Uchiyama K, Shaw A, Zhang X and Freemont PS (2004) Structural basis of the interaction between the AAA ATPase p97/VCP and its adaptor protein p47. *EMBO J* **23**, 1030–1039.

Supporting information

Additional supporting information may be found in the online version of this article at the publisher's web site:

Fig. S1. MS analysis of p97 after recombinant expression and purification in nucleotide-free buffer.
Fig. S2. Hierarchical classification focused on the N-domains of protomers.
Fig. S3. Non-symmetrized ADP, AMP-PNP and ATP-γSdensities.
Fig. S4. Rotational symmetry analysis of the reconstructions.
Fig. S5. Resolution assessment of reconstructions.
Fig. S6. Domain specific FCR analysis of fitted atomic models, related to Figure 3.